Weyl–Kondo semimetal behavior in the chiral structure phase of $Ce_3Rh_4Sn_{13}$

Kazuaki Iwasa,[1,2,*] Kazuya Suyama,[3] Seiko Ohira-Kawamura,[4] Kenji Nakajima,[4] Stéphane Raymond,[5] Paul Steffens,[6] Akira Yamada,[7] Tatsuma D. Matsuda,[7] Yuji Aoki,[7] Ikuto Kawasaki,[8] Shin-ichi Fujimori,[8] Hiroshi Yamagami,[9,8] and Makoto Yokoyama[2]

[1]*Frontier Research Center for Applied Atomic Sciences, Tokai, Naka, Ibaraki 319-1106, Japan*
[2]*Institute of Quantum Beam Science, Ibaraki University, Mito, Ibaraki 310-8512, Japan*
[3]*Department of Physics, Tohoku University, Sendai, Miyagi 980-8578, Japan*
[4]*Materials and Life Science Division, J-PARC Center, Japan Atomic Energy Agency, Tokai, Ibaraki 319-1195, Japan*
[5]*University Grenoble Alpes, CEA, IRIG, MEM, MDN, 38000 F-Grenoble, France*
[6]*Institut Laue-Langevin, BP 156, 38042 Grenoble Cedex 9, France*
[7]*Department of Physics, Tokyo Metropolitan University, Hachioji, Tokyo 192-0397, Japan*
[8]*Materials Sciences Research Center, Japan Atomic Energy Agency, Sayo, Hyogo 679-5148, Japan*
[9]*Department of Physics, Faculty of Science, Kyoto Sangyo University, Kyoto 603-8555, Japan*

(Received 3 October 2022; accepted 16 December 2022; published 9 January 2023)

The spin dynamics, crystalline-electric-field (CEF) level scheme, specific heat, and x-ray photoemission spectra (XPS) of $Ce_3Rh_4Sn_{13}$ were investigated, which exhibits anomalous semimetal transport in the chiral crystallographic phase. CEF excitations observed at approximately 7 and 39 meV are consistent with the two inequivalent Ce-ion cites in the chiral structure. Because of broader CEF excitations and a strong $4f^1$ peak at the Fermi level in the Ce $4f$ on-resonance spectrum, the hybridized Ce $4f$ electrons contribute to the semimetal carriers. In addition, the spin fluctuation associated with the Kramers doublet ground state is characterized by the peak located at 0.15 meV. The electronic state involving the spin fluctuation causes the T^3 behavior of specific heat below 0.6 K, which is attributed to linear dispersion relations of electrons of the Weyl–Kondo semimetal in the chiral-lattice symmetry.

DOI: 10.1103/PhysRevMaterials.7.014201

I. INTRODUCTION

The Kondo effect has been a central issue in the study on electronic quantum many-body effects [1,2]. Recently, the Kondo semiconductors or semimetals appearing in the case of half-filling condition for the band structure have been investigated in the context of topological insulators [3–5]. In particular, the chiral symmetry and noncentrosymmetry are considered to provide the Weyl fermion owing to the anisotropic spin-orbit interaction [6,7]. The Weyl–Kondo semimetal, in which the Weyl fermion carriers are active within the Kondo hybridization state [8,9], has been proposed for the noncentrosymmetric $Ce_3Bi_4Pd_3$ [10,11]. The T^3 behavior in the low-temperature specific heat and the spontaneous Hall effect are considered to be evidences for such a correlated-electron topological state. The effect of Weyl fermion to the Ruderman–Kittel–Kasuya–Yoshida (RKKY) interaction was also discussed [12,13]. It is a broad and current interest to investigate Weyl fermion states caused by combinations of the quantum many-body effects and the characteristic symmetry effects.

The $Ce_3T_4Sn_{13}$ (T = Co, Rh, and Ir) compounds have been hypothesized to be Kondo-effect materials [14–24]. The large values of specific heat divided by the temperature (C_p/T) in the low-temperature region were considered to be signatures of heavy fermions (HF). It is remarkable that the electrical resistivity data of $Ce_3T_4Sn_{13}$ (T = Co, Rh, and Ir) show less temperature dependencies and much higher values compared to the isomorphic superconductors $La_3T_4Sn_{13}$ (T = Co, Rh, and Ir) [15,20,25–27]. These electronic properties indicate that the Ce-based compounds are Kondo semimetals. Recently, the inelastic neutron scattering (INS) measurement for $Ce_3Co_4Sn_{13}$ revealed the spin excitation in the energy range near 0.2 meV [28] without magnetic ordering even at 0.4 K [29]. Previous studies on $Ce_3Rh_4Sn_{13}$ reported the magnetic ordering below 1.2 K, which was deduced from the specific-heat peaks [19]. However, a recent neutron diffraction study did not evidence clear long-range magnetic order even at 50 mK [30]. $Ce_3Ir_4Sn_{13}$ undergoes an antiferromagnetic (AFM) phase transition at $T_N = 0.6$ K, whereas the magnitude of the ordered magnetic moment was estimated to be of the order of 0.1 μ_B/Ce [31]. The Ir-based material also exhibits the spin excitation near 0.2 meV [32]. Such a low energy scale for magnetic fluctuation is consistent with the the magnetic entropy value of 1 J/(K mol Ce) ($0.17R \ln 2$) at T_N, where R denotes the gas constant [23]. These results indicate the weak ordered state of $Ce_3T_4Sn_{13}$ (T = Co, Rh, and Ir), which are characterized by strong spin fluctuation at approximately 0.2 meV as evidenced by previous INS measurements.

The crystal structures of $Ln_3T_4Sn_{13}$ (Ln = La and Ce, T = Co, Rh, and Ir) have been controversial as summarized in the

*kazuaki.iwasa.ifrc@vc.ibaraki.ac.jp

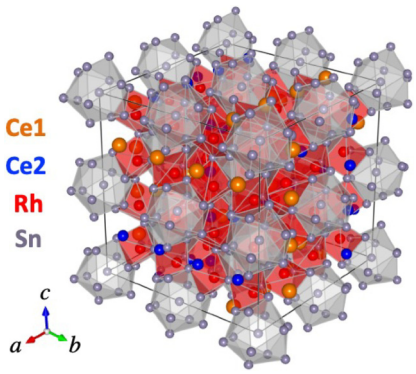

FIG. 1. Schematic of crystal structure of an enantiomer of $Ce_3Rh_4Sn_{13}$ in the chiral I′ phase [30]. The Sn atoms form the cagelike unit shown by the shaded polyhedra, and the Rh atoms are located between them (red prisms). The two inequivalent Ce ions, Ce1 and Ce2, as shown by the orange and blue circles, respectively. The view was drawn using VESTA [47].

Supplemental Material [33] (see also Refs. [34–43] therein). At the early stage of the study of this compound series, $La_3Rh_4Sn_{13}$ and $Ce_3Rh_4Sn_{13}$ were suggested to crystallize in the $I4_132$ space group (No. 214) [44,45]. Recently, based on the precise analysis of synchrotron x-ray diffraction data for the single-crystalline samples synthesized using the molten-Sn flux method, $Ln_3T_4Sn_{13}$ (Ln = La and Ce, T = Co, Rh, and Ir) are concluded to show a transformation from the crystal structure with the space group $Pm\bar{3}n$ (I phase, lattice constant $a = 9.6$–9.7 Å) to the chiral noncentrosymmetric structure with $I2_13$ (I′ phase, lattice constant $a' = 19.2$–19.4 Å) at $T_D \simeq 160$, 350, and 600 K, respectively [30–32,46]. One of the enantiomers of the I′-phase chiral structure of $Ce_3Rh_4Sn_{13}$ is shown in Fig. 1, which was drawn using VESTA [47]. The Ce-ion sites split into two inequivalent Wyckoff sites depicted by Ce1 and Ce2, which form linear arrays along the cubic principal axes as indicated by the orange and blue circles. The INS studies on $Ce_3Co_4Sn_{13}$ and $Ce_3Ir_4Sn_{13}$ evidenced that the Ce1 and Ce2 ions carry different crystalline-electric-field (CEF) split levels [28,32]. These two-level schemes show different spectral widths; thus, the Kondo hybridization with conduction electrons is not uniform. Because the bulk chiral fermion and the Weyl semimetallic state are suggested to be protected by the $I2_13$ space group [6], we hypothesize that the hybridization between the Ce $4f$ electrons and the conduction electrons (c-f hybridization) tune the Fermi level at the band crossing points, resulting in the low-carrier semimetal state. Thus, the Weyl–Kondo strongly correlated electrons in the chiral symmetry lattice can be examined in $Ce_3T_4Sn_{13}$ (T = Co, Rh, and Ir).

The present study aims at revealing the Ce $4f$ electron state relevant to the anomalous semimetal behavior in the chiral structure phase of $Ce_3Rh_4Sn_{13}$. As a result, the INS excitations located at approximately 7 and 39 meV are both the combination of sharp and broad peaks that are explained by two inequivalent CEF level schemes corresponding to the Ce1 and Ce2 sites. The spin fluctuation associated with the Kramers doublet ground states appears at approximately 0.15 meV, which contributes to the T^3 behavior of the specific heat in the lower-temperature region below approximately 1 K. The XPS result supports the contribution of the Ce $4f$ state to the Fermi level as a consequence of electronic hybridization. We discuss the possible Weyl–Kondo fermions in $Ce_3Rh_4Sn_{13}$.

II. EXPERIMENTAL DETAILS

Samples of $Ln_3Rh_4Sn_{13}$ (Ln = La and Ce) were synthesized via the molten Sn-flux method from R (3N), Rh (4N), and Sn (5N) starting materials [15,34,48,49]. We succeeded in obtaining single crystals with maximum dimensions of 5 mm.

INS experiments for samples powdered from the fine single crystals were performed by using the pulsed-cold-neutron disk chopper spectrometer AMATERAS installed at the beamline BL14 of the Materials and Life Science Experimental Facility (MLF), J-PARC [50]. We measured the spectra of $Ln_3Rh_4Sn_{13}$ (Ln = La and Ce) specimens with the same mass, and extracted the $4f$-electron contribution from the difference between the data of these two compounds. The incident neutron energies of $E_i = 3.44$, 8.97, and 60.4 meV were selected via the chopper combination with the energy resolutions of 0.057, 0.26, and 3.77 meV, respectively, corresponding to the full width at half-maximum at the elastic scattering positions. The Utsusemi software suite was used to analyze the time-of-flight (ToF) neutron spectral data [51].

INS experiments were also performed for nine coaligned single-crystalline samples of $Ce_3Rh_4Sn_{13}$ on the ThALES cold-neutron triple-axis spectrometer at the reactor of Institut Laue-Langevin. The crystalline axes [1 0 0] and [0 1 1] were on the horizontal scattering plane, and the coaligned sample mosaic is approximately 4 deg. A pyrolytic graphite monochromator and analyzer were used, and the energy resolution at the elastic scattering condition was 0.10 meV with the detected final neutron energy fixed at $E_f = 3.5$ meV. Measurements were conducted using incident-neutron constant monitor counts.

The sample temperatures were controlled using a ^{3}He closed-cycle refrigerator and a liquid-helium cryostat for AMATERAS and ThALES, respectively.

Specific heat of $Ce_3Rh_4Sn_{13}$ was measured by using a relaxation method with Quantum Design PPMS down to 0.41 K installed at Department of Physics, Tokyo Metropolitan University. The single-crystal samples with the masses of 0.167 and 5.253 mg were used for the measurements in different temperature ranges. Magnetic fields were applied up to 9 T along the [1 0 0] axis of the single-crystal samples.

Measurements of x-ray absorption spectroscopy (XAS) and x-ray photoemission spectroscopy (XPS) were conducted at the soft x-ray undulator beamline BL23SU of SPring-8. The x-ray energy range between 855 and 911 eV, which includes the Ce $3d$ absorption edges (860 and 881 eV), was used to investigate the Ce $4f$-electron state. The binding energy of photoelectron was evaluated with respect to the Fermi edge of a gold film. The single crystal sample was cleaved in a vacuum chamber, and was transported to the beamline at which sample temperature was cooled to 20 K using a liquid-helium-flow cryostat.

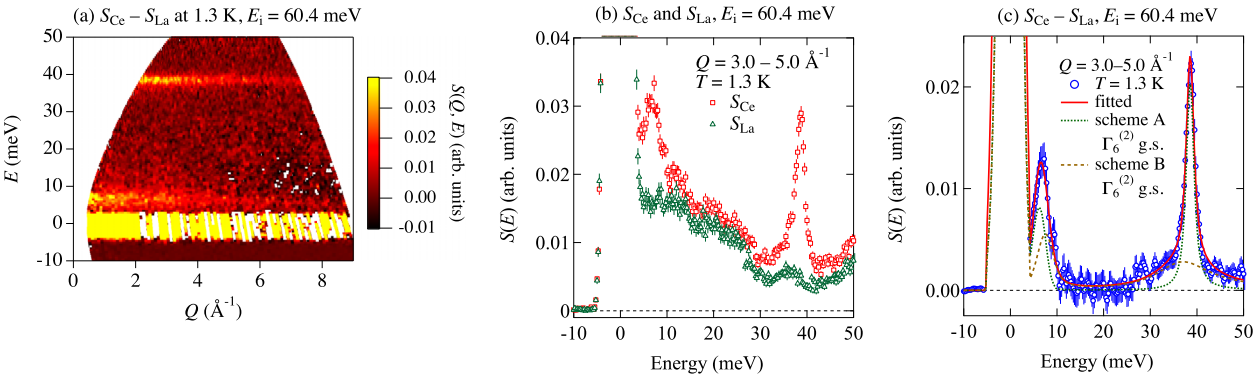

FIG. 2. (a) Magnetic $S(Q, E)$ contour map for $Ce_3Rh_4Sn_{13}$ at 1.3 K. The incident neutron energy is $E_i = 60.4$ meV. The result was obtained by subtracting the data of the reference material, $La_3Rh_4Sn_{13}$ [33]. (b) Scattering function data of $Ce_3Rh_4Sn_{13}$ (S_{Ce} with red squares) and $La_3Rh_4Sn_{13}$ (S_{La} with green triangles) at 1.3 K, which correspond to integration of intensity in the range of $Q = 3.0-5.0$ Å^{-1}. (c) Magnetic $S(E)$ at 1.3 K (open symbols) after subtracting the corrected La data from the Ce data. The red solid line is a fitted result of the CEF-excitation calculation with the two inequivalent schemes (a green dotted line for A and a brown broken line for B).

III. RESULTS

A. ToF INS results

In this section we will show the ToF INS results for the $Ce_3Rh_4Sn_{13}$ powdered sample, which was subsequently used for an analysis of the Ce $4f$-electron CEF schemes and of the spin fluctuations in the low-energy range.

Figure 2(a) shows a contour map of the magnetic scattering function $S(Q, E)$ at 1.3 K obtained from the INS intensity measured with $E_i = 60.4$ meV. The result was obtained by subtracting the data of the reference material $La_3Rh_4Sn_{13}$, the crystal structure of which was confirmed to be the same as the $I2_13$ structure of $Ce_3Rh_4Sn_{13}$ based on the recent precise analysis of synchrotron x-ray diffraction data [30]. To deduce magnetic scattering intensity owing to the Ce $4f^1$ state, the intensity corrections for the La-sample data was performed to evaluate a nuclear scattering (phonon) component, the details of which are described in the Supplemental Material [33] (see also Refs. [52–54] therein). The extracted magnetic scattering cross section of the Ce $4f$ electrons is composed of the strong intensities appearing clearly at 6.9 and 38.6 meV, which are consistent with the previously reported INS energy spectrum [55]. The peak energies are independent of the magnitude of the scattering wave vector Q, while the intensity decreases monotonically with increased Q. The intensity dependence on Q follows the squared magnitude of the magnetic form factor of the Ce^{3+} $4f^1$ electronic state. This result indicates that the observed INS peaks correspond to the magnetic scattering owing to the transitions between the CEF levels of the Ce $4f$ electrons.

Figure 2(b) shows the raw data S_{Ce} of $Ce_3Rh_4Sn_{13}$ (red squares) and S_{La} of $La_3Rh_4Sn_{13}$ (green triangles) at 1.5 K, which were evaluated via intensity integration over the results obtained for the range of $Q = 3.0-5.0$ Å^{-1} in the intensity contours. As described above, the inelastic peaks are seen at 6.9 and 38.6 meV. As described in the Supplemental Material, the S_{La} was corrected to estimate phonon background, and the result is subtracted from S_{Ce} [33]. The resultant magnetic $S(E)$ component owing to the Ce $4f^1$ state was extracted as shown by blue circles in Fig. 2(c). The sharp peak at 6.9 meV is followed by a tail extending to 10 meV, and broad intensities extend over the energy range above 25 meV beyond the sharp peak at 38.6 meV. Because of the sharp and broad spectra, the $4f$ electrons behave as either well localized to the Ce ion or hybridized with conduction electrons. Similar INS peaks composed of the sharp and broad spectra were also detected in I′ phase of $Ce_3Co_4Sn_{13}$ [28] and $Ce_3Ir_4Sn_{13}$ [32]. The result was explained by the two inequivalent CEF schemes for the independent Ce-ion sites in the chiral lattice. Since $Ce_3Rh_4Sn_{13}$ also takes the same chiral lattice, the $S(E)$ spectrum should be composed of the two $4f$ electron states, which will be discussed later in detail.

Figure 3 shows the $S(E)$ result for the $E_i = 8.97$ meV setup, which was obtained using the analysis with subtraction of $S_{La}(E)$ from $S_{Ce}(E)$ evaluated by intensity integration in the range of $Q = 1.5-2.5$ Å^{-1} [33]. This high-resolution measurement reveals the sharp component at 6 meV and the intensity extending to the higher energy. Such asymmetric spectrum supports the two scattering intensity components as proposed above. Moreover, we detected low-energy scattering intensity apparent below 2 meV, which is enhanced with

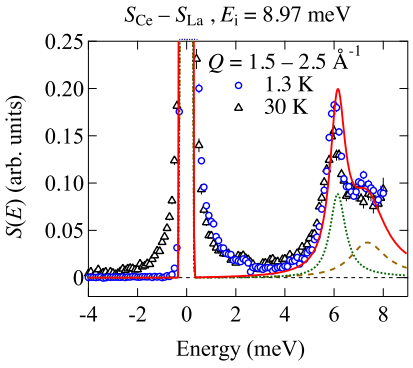

FIG. 3. Magnetic $S(E)$ spectra for $Ce_3Rh_4Sn_{13}$ at 1.3 and 30 K measured using $E_i = 8.97$ meV, which were evaluated by intensity integration in the range of $Q = 1.5-2.5$ Å^{-1}. The data correspond to the spectral difference between the Ce- and La-based compounds [33]. The red solid line is a fitted result of the CEF-excitation analysis with the two inequivalent schemes (green dotted line for A and brown broken line for B) for the $E_i = 60.4$ meV data.

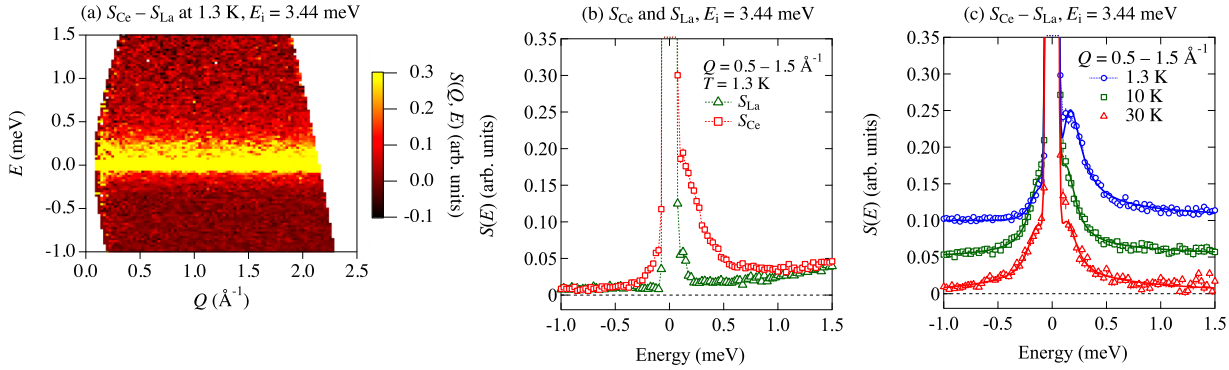

FIG. 4. (a) Magnetic $S(Q, E)$ contour map for $Ce_3Rh_4Sn_{13}$ powdered sample at 1.3 K using $E_i = 3.44$ meV. The data set corresponds to the spectral difference between the Ce- and La-based compounds [33]. (b) $S(E)$ data of $Ce_3Rh_4Sn_{13}$ (S_{Ce} with red circles) and $La_3Rh_4Sn_{13}$ (S_{La} with green triangles) at 1.3 K obtained by intensity integration in the range of $Q = 0.5$–1.5 Å^{-1}. (c) $S(E)$ data at 1.3, 10, and 30 K obtained by intensity integration in the range of $Q = 0.5$–1.5 Å^{-1} shown in (a). Each temperature data set is shifted by 0.05 along the ordinate. Solid lines are fitted results based on the dynamical susceptibility $\chi''_S(\boldsymbol{Q}_{avr}, E)$.

decreasing temperature from 30 to 1.3 K. The temperature dependence can be attributed to magnetic excitation in the material.

Figure 4(a) shows the low-energy $S(Q, E)$ map obtained at 1.3 K using $E_i = 3.44$ meV, which was obtained from the intensity difference between the Ce- and La-sample data [33]. In addition to strong incoherent scattering at $E = 0$, we detected intensity in the positive E region without any clear Q dependence. Symbols of Fig. 4(b) shows $S(E)$ at 1.3 K of $Ce_3Rh_4Sn_{13}$ (red circles) and $La_3Rh_4Sn_{13}$ (green triangles) obtained by integration of intensity in the range of $Q = 0.5$–1.5 Å^{-1}. Clear intensity difference appears between them, which corresponds to the magnetic $S(E)$ shown in Fig. 4(a). Symbols of Fig. 4(c) show the magnetic $S(E)$ with intensity integration in the range of $Q = 0.5$–1.5 Å^{-1} at the selected temperatures, which were derived from Fig. 4(a). Clear inelastic spectra were observed below ∼1 meV, which are consistent with the magnetic scattering as discussed above for the $E_i = 8.97$ meV data. The previous INS studies on $Ce_3T_4Sn_{13}$ (T = Co, Rh, and Ir) also revealed such a low-energy response [28,29,32,55]. Therefore, the CEF ground state of the $Ce_3T_4Sn_{13}$ compounds provides the spin fluctuation whose characteristic energy is 0.1–0.2 meV. The CEF level sequence is determined by charge potential from ligand ions and electronic hybridization potential, which was studied for the metal-nonmetal transition associated with the totally symmetric multipolar ordering in $PrRu_4P_{12}$ [56–58].

B. Triple-axis-spectrometer INS results

A detailed INS investigation for the single-crystalline sample was also conducted using the triple-axis spectrometer ThALES at ILL [59]. The measured spectra at $\boldsymbol{Q} = (3, 0, 0)$ is shown in Fig. 5(a). Here the reciprocal lattice unit is defined as $2\pi/a'$ with $a' = 19.4$ Å for I′ phase. Small symbols near $E = 0$ with the right ordinate are elastic scattering, which show the energy resolution of 0.1 meV. The intensities measured at 1.6 K, shown by blue open circles with the left ordinate, are enhanced above the energy of elastic scattering tail to 0.4 meV compared to the 20-K data shown by red solid squares. This behavior is consistent with the ToF powdered sample result. Figure 5(b) shows scan profiles along the symmetrical reciprocal-lattice lines [1, 0, 0], [1, 1, 1], and [0, 1, 1] with the fixed energy transfer of 0.25 meV. Blue and red open symbols are raw data measured at 1.6 and 20 K, respectively, and the data at 40 K are shown by black diamonds. The intensity at 1.6 K is stronger than in the other temperature data. Solid symbols are intensity difference with respect to the 40-K data. The red solid squares measured at 20 K are located near null intensity, whereas the blue solid circles for 1.6 K are at nonzero positive magnitude. The intensity at 1.6 K does not exhibit any particular Q dependence. This feature is also consistent with the powdered-sample ToF data shown in Fig. 4(a); the scattering intensity in the $E > 0$ region seems to be uniform along the Q direction. The observed result is a signature that the spin fluctuation is a local excitation, not a collective mode, at 1.4 K. It is in contrast to the dispersion relation of the 0.2-meV magnetic excitation in $Ce_3Co_4Sn_{13}$ at 1.5 K [28], whereas the magnetic fluctuation of $Ce_3Ir_4Sn_{13}$ is rather similar to the $Ce_3Rh_4Sn_{13}$ case [32].

C. Specific heat

Figure 6 shows specific heat divided by temperature (C_p/T) as a function of squared temperature under the magnetic fields of $\mu_0 H = 0$, 3, 6, and 9 T applied along the [1 0 0] axis of the single-crystal samples. A broad maximum peak appears at $T^2 \simeq 0.8$ K^2 under zero magnetic field, and moves to a higher-temperature side with increasing magnetic fields. The temperature dependence and the magnetic-field dependence are consistent with the previous investigations [20,21].

According to the specific-heat investigation by Köhler *et al.* [20], the low-temperature C_p value of $Ce_3Rh_4Sn_{13}$ at 2 K under the zero magnetic field is dominated by the magnetic component because the C_p of $La_3Rh_4Sn_{13}$ is much less than that of $Ce_3Rh_4Sn_{13}$. This study also investigated the rattling-like atomic vibration characterized by the energy of 4.48 meV of Sn atoms located inside the cage structure. However, no significant contribution of such an atomic motion is seen below 2 K not only in the C_p data of $Ce_3Rh_4Sn_{13}$ but also in $La_3Rh_4Sn_{13}$. Thus, it is conclusive that the specific heat

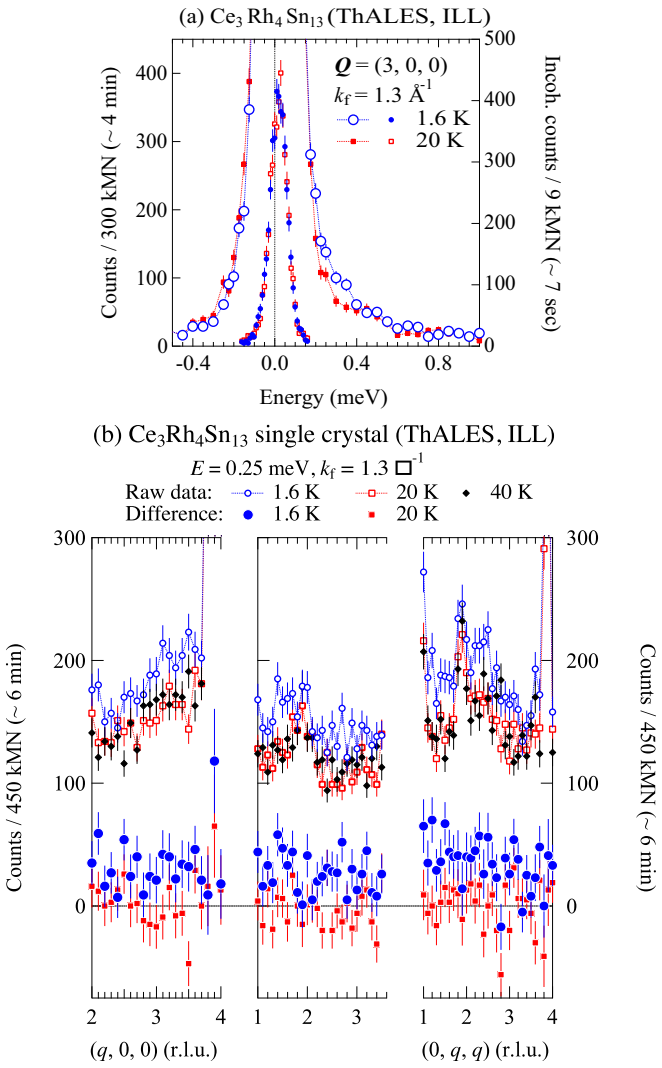

FIG. 5. (a) Triple-axis INS spectra at $\boldsymbol{Q} = (3, 0, 0)$ of the single crystal sample of $Ce_3Rh_4Sn_{13}$ measured at 1.6 (blue symbols) and 20 K (red symbols). Small symbols near $E = 0$ with the right ordinate are elastic scattering to show the energy resolution, and larger symbols are the inelastic part with the left ordinate. (b) Several scans with the fixed energy transfer of 0.25 meV along the symmetrical reciprocal-lattice lines at 1.6, 20, and 40 K. Blue and red open symbols are raw data at 1.6 and 20 K, respectively, and solid symbols shown by black diamonds are intensity difference with respect to the 40-K data. The reciprocal lattice unit is defined as $2\pi/a'$ with $a' = 19.4$ Å for I′ phase.

of $Ce_3Rh_4Sn_{13}$ shown in Fig. 6 is attributed to the electronic (magnetic) contribution. The previous study explained that the large C_p/T value below 2 K is caused by the Kondo interactions. In addition, the broad peak at 1 K was proposed to be a signature of short-range magnetic order. However, as described above for the INS intensity independent of Q, no clear spatial magnetic correlation emerges, although the measuring temperature of 1.3 K is above the C_p/T peak. We will discuss these specific-heat data in terms of the Weyl–Kondo semimetal electron that is expected to be relevant to the spin fluctuation.

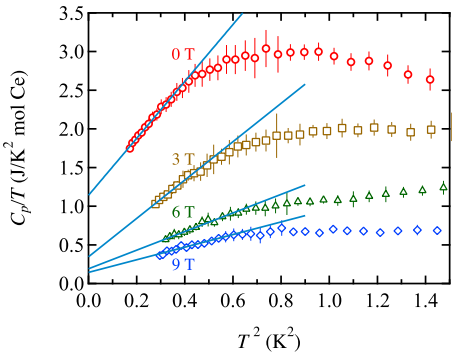

FIG. 6. Symbols are specific heat divided by temperature (C_p/T) under the several magnetic fields. Lines are fitted linear functions ($C_p/T = \gamma + \beta' T^2$) to the low-temperature regions.

D. X-ray photoemission spectroscopy

Figure 7 shows XAS and XPS spectra of $Ce_3Rh_4Sn_{13}$ at 20 K. The XAS spectrum shown in Fig. 7(a) consists of the Ce $3d_{5/2}$ and $3d_{3/2}$ components, and each of them is assigned as the $4f^2$ final state peak. The $4f^1$ final state peaks, which should be located at around 887 eV ($3d_{5/2}$) and 905 eV ($3d_{3/2}$), are not observed in the XAS spectrum [60]. The $4f^1$ final state peak originates from the transition from the $4f^0$ ground state, and its absence in the XAS spectrum claims that the number of $4f$ state n_{4f} is very close to unity. This is consistent with the result of the previous core-level XPS spectroscopy study of this compound [17]. Black and red arrows indicate energies selected for the XPS measurements shown in Figs. 7(b) and 7(c). Black squares in Figs. 7(b) and 7(c) are the XPS data obtained using the x-ray energy at 860 eV corresponding to the off-resonance energy. The spectrum centered at the binding energies of 3 eV is considered to be dominated by the Rh and Sn electronic state, as observed in a previous study [17]. Red circles are data obtained using the x-ray energy at 881 eV of the Ce $3d$ $j = 5/2$ absorption-edge energy for the $3d$-$4f$ on-resonance condition, and the valence band spectrum is dominated by the contribution from the Ce $4f$ states. There are two peaks located at 2.5 and 0.22 eV, which are attributed to the $4f^0$ and $4f^1$ states, respectively. As seen in Fig. 7(c) showing the spectra close to the zero binding energy, the tail of $4f^1$-state peak crosses the Fermi energy (zero binding energy), which indicates that the $4f$ electrons hybridize with conduction electrons, and contribute to the Fermi surface.

IV. ANALYSIS

A. CEF analysis of the ToF data

The INS spectrum at 1.3 K measured using the $E_i = 60.4$ meV setup was analyzed on the basis of the CEF-split schemes for Ce $4f$ electrons. The previous study on $Ce_3Rh_4Sn_{13}$ adopted the single CEF scheme [55], but it should be reexamined using the two CEF schemes because the I′-phase structure (the $I2_13$ space group) contains the two inequivalent Wyckoff Ce-ion sites [30]. The local symmetry at the Ce-ion site in the I′-phase structure becomes lower than the D_{2d} point group for the I phase ($Pm\bar{3}n$) above T_D.

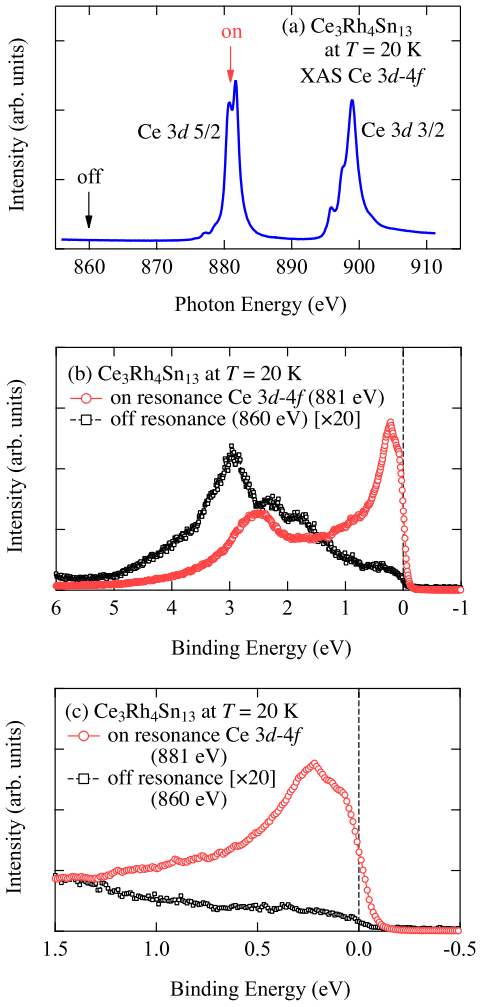

FIG. 7. (a) XAS spectrum near the Ce 3*d* $j = 5/2$ and 3/2 absorption edges of $Ce_3Rh_4Sn_{13}$ at 20 K. (b) XPS spectra of $Ce_3Rh_4Sn_{13}$ at 20 K. Red circles and black squares are data obtained at the 3*d*-4*f* resonance position [red arrow in (a)] and the off-resonance position [black arrow in (a)], respectively. (c) The XPS data near the Fermi energy.

However, the additional CEF Hamiltonian terms are expected to be less effective compared to those of D_{2d} because of the small atomic displacements across T_D; thus, the CEF Hamiltonian is assumed to be expressed by the D_{2d} form as

$$\mathcal{H}_{\rm CEF} = W\left[\frac{x_1}{2}O_2^0 + \frac{x_2}{60}O_4^0 + \frac{1-|x_1|-|x_2|}{12}O_4^4\right], \quad (1)$$

where the O_m^n are Stevens operators [61]. Using a set of basis wave functions for the total angular momentum $J = 5/2$ for the Ce^{3+} $4f^1$ configuration, we have diagonalized this Hamiltonian to obtain eigenfunctions of the three Kramers doublets, $\Gamma_6^{(1)}$, $\Gamma_6^{(2)}$, and Γ_7. The scattering function is expressed as $S(Q,E) = [n(E)+1]\chi''_{\rm CEF}(Q,E)$, where $\chi''_{\rm CEF}(Q,E)$ is the imaginary part of the generalized magnetic susceptibility and $n(E)$ is the Bose-Einstein distribution function. According to Marshall and Lowde [62], $\chi''_{\rm CEF}(Q,E)$ for the CEF splitting state is represented by

$$\chi''_{\rm CEF}(Q,E) \propto f^2(Q)E\frac{1}{Z}\left[\sum_{m,n}^{(E_m=E_n)}|\langle n|\boldsymbol{J}_\perp|m\rangle|^2\frac{e^{-\frac{E_m}{k_BT}}}{k_BT}F_{mn}(E) + \sum_{m,n}^{(E_m\neq E_n)}|\langle n|\boldsymbol{J}_\perp|m\rangle|^2\frac{e^{-\frac{E_m}{k_BT}}-e^{-\frac{E_n}{k_BT}}}{E_n-E_m}F_{mn}(E)\right], \quad (2)$$

where $f(Q)$ is the magnetic form factor. E_m and E_n are the respective energy eigenvalues of the initial and final states, $|m\rangle$ and $|n\rangle$, which are relevant to the scattering process due to the dipole operator $\boldsymbol{J}_\perp$. Z is the partition function. We assumed the Lorentzian spectral function $F_{mn}(E) = \gamma_{mn}/[(E-\Delta_{mn})^2+\gamma_{mn}^2]$, with $\Delta_{mn} = E_n - E_m$. A least-squares fitting based on the two schemes A and B both represented by Eq. (2) and the Lorentzian $F_{mn}(E)$ to the obtained data was performed. In order to evaluate the excitation-peak width, we incorporated a procedure for convolution of the spectrometer resolution, which was estimated by fitting the $E = 0$ incoherent-scattering part before performing the INS part analysis. The resolution at $E > 0$ was simply assumed to be proportional to $(1 - E/E_i)^{3/2}$ [63,64].

In previous studies on the CEF levels located near 7 and 40 meV in $Ce_3Co_4Sn_{13}$ [28] and $Ce_3Ir_4Sn_{13}$ [32], we performed a systematic search for the CEF-level schemes within the space of the two sets of CEF parameters, W, x_1, and x_2, to reproduce the two major excitation peaks. We hypothesized a constraint of the same site multiplicity for Ce1 and Ce2 in the I′ phase. In addition, the sharp CEF excitation peaks should be produced by the one Ce-ion site, and the broad response by the another Ce-ion site. Based on the CEF spectral analysis, we discussed the different hybridization effects at Ce1 and Ce2 in the I′ phase of $Ce_3Co_4Sn_{13}$ and $Ce_3Ir_4Sn_{13}$. Therefore, in the present study, we applied the same analysis procedure to the data of $Ce_3Rh_4Sn_{13}$. The CEF parameters were found to favor the $\Gamma_6^{(2)}$ ground state. Although the INS peaks at 7 and 39 meV of $Ce_3Rh_4Sn_{13}$ do not show clear splitting expected for the two Wyckoff sites of the Ce ions, the determined CEF-excitation spectrum of $Ce_3Rh_4Sn_{13}$ at 1.3 K is well reproduced by the fitted results shown by the lines in Fig. 2(c). The resultant $\mathcal{H}_{\rm CEF}$ parameters, the eigenstates, the energy eigenvalues, and the spectral widths are listed in Table I. The CEF parameter set, scheme A, gives the result indicated by the green dotted line in Fig. 2(b). The parameter set, scheme B, corresponds to the brown broken line. Both schemes A and B are comprised of the sequence $\Gamma_6^{(2)}$ (ground state)–Γ_7–$\Gamma_6^{(1)}$. The spectral widths γ for the first excited states are 0.1 and 0.8 meV for the CEF parameter sets of schemes A and B, respectively, and those for the second excited states are 0.9 and 7 meV, respectively. The calculated relative inaccuracy of the width parameters in the fitting analysis are large because of the spectral overlapping between schemes A and B. However, the peak positions in A and B schemes are resolved, and the spectrum in scheme A is sharper and that in scheme B is broader. To confirm validity of the CEF scheme analysis for the $E_i = 60.4$ meV setup data, we calculated a $S(E)$ spectrum for $E_i = 8.97$ meV setup using the same CEF parameter set (Table I). The width

TABLE I. The CEF parameters (W, x_1, x_2), the eigenstates together with the energy eigenvalues ($E_{\rm CEF}$), and the spectral widths (γ) determined by the least-squares fitting analysis for the data sets at 1.3 K obtained by the $E_{\rm i} = 60.4$ meV data set.

CEF scheme	A	B
W (meV)	11.82(1)	10.9(2)
x_1	0.100(2)	0.08(1)
x_2	−0.171(1)	−0.17(1)
Ground state (g.s.)	$\Gamma_6^{(2)}$	$\Gamma_6^{(2)}$
First ex. state and $E_{\rm CEF}$ (meV)	Γ_7 6.14	Γ_7 7.31
Second ex. state and $E_{\rm CEF}$ (meV)	$\Gamma_6^{(1)}$ 38.5	$\Gamma_6^{(1)}$ 36.4
γ_{01} (meV) [g.s. → first]	0.1(3)	0.9(9)
γ_{02} (meV) [g.s. → second]	0.8(2)	7(1)

parameters $\gamma_{01} = 0.375$ and 0.9 meV were fixed for A and B schemes, respectively, to compare with the experimental data. The calculated result is shown by lines in Fig. 3. The red solid line is the total scattering function, which is consistent with the experimental data showing a sharp peak at 6 meV followed by a shoulderlike intensity near 7 meV. The green dotted and brown broken lines are components of scheme A and B, respectively. Because of the inaccuracy of fitting parameters to the $E_{\rm i} = 60.4$ meV data, we see a slight discrepancy between the measured data and the calculation, but the two-scheme model with the sharp A and broad B is concluded to be valid for the $4f$-electron state in $Ce_3Rh_4Sn_{13}$.

We compare hereafter the fitted result for CEF schemes of $Ce_3Rh_4Sn_{13}$ with those of $Ce_3Co_4Sn_{13}$ [28] and $Ce_3Ir_4Sn_{13}$ [32]. The first and second excited levels of the three compounds are located in the same energy ranges. However, only $Ce_3Co_4Sn_{13}$ shows the switch of the ground state from $\Gamma_6^{(2)}$ to Γ_7 across the chiral structure transformation, which can be attributed to stronger CEF potential owing to the shorter interatomic distances. The spectral width for the $\Gamma_6^{(2)}$-$\Gamma_6^{(1)}$ excitation of the B scheme in $Ce_3Rh_4Sn_{13}$ is broader than that of $Ce_3Co_4Sn_{13}$ ($\gamma = 3.83$ meV) and $Ce_3Ir_4Sn_{13}$ ($\gamma = 4$ meV). Such marked broadening in the B scheme of $Ce_3Rh_4Sn_{13}$ is a signature of a strong effect of c-f hybridization, while the relatively well-localized Ce-ion sites give the sharp A scheme. According to the solved crystal structure in the I′ phase shown in Fig. 1, the averaged nearest-neighbor distances between Ce1 and Sn is 3.390 Å, while that between Ce2 is 3.441 Å. The broader spectral widths of scheme B can be attributed to the Ce1 site having shorter interatomic distances to the surrounding Sn because c-f hybridization is expected to be stronger for the shorter atomic distance. The CEF level sequence is determined by charge potential from ligand ions and electronic hybridization potential, which was studied for the metal-nonmetal transition associated with the totally symmetric multipolar ordering in $PrRu_4P_{12}$ [56–58]. It is a further issue to discuss the hybridization effect on the revealed CEF sequences of $Ce_3T_4Sn_{13}$ (T = Co, Rh, and Ir) by considering the detailed crystal structures.

B. Low-energy INS spectral analysis

We also analyze the low-energy INS data of the powdered sample measured at the ToF spectrometer AMATERAS. As described above, the clear excitation signal below approximately 0.5 meV was enhanced below 15 K, which can be ascribed to the spin dynamics relevant to the Kramers doublet CEF ground state. To extract the characteristic physical quantities, we performed a least-squares fitting analysis to the data shown in Fig. 4(c). The spectral-function form was based on the dynamical susceptibility with the single-pole approximation and the finite excitation energy [65] represented as

$$S(E) = [n(E)+1]\chi_{\rm S}''(\boldsymbol{Q}_{\rm avr}, E) = \frac{1}{1-e^{-E/k_{\rm B}T}}\frac{E}{2\pi} \times A\left[\frac{\Gamma}{(E-E_0)^2+\Gamma^2} + \frac{\Gamma}{(E+E_0)^2+\Gamma^2}\right], \quad (3)$$

together with a Gaussian form for the elastic peak. The fitted results are represented by solid lines in Fig. 4(c). The determined parameters A, E_0, and Γ are plotted in Fig. 8 as functions of temperature. The A parameter is enhanced with decreasing temperature, which is consistent with the static magnetic susceptibility reported in the previous studies [30]. The E_0 value is located at approximately 0.12 meV, and increases slightly to 0.15 meV with decreasing temperature below 5 K within the measurement accuracy. This characteristic energy of $Ce_3Rh_4Sn_{13}$ is close to 0.2 meV for $Ce_3Co_4Sn_{13}$ [28] and 0.1 meV for $Ce_3Ir_4Sn_{13}$ [32]. The spectral width value Γ of $Ce_3Rh_4Sn_{13}$ is approximately 0.1 meV, which is also in the same order of those of $Ce_3Co_4Sn_{13}$ and $Ce_3Ir_4Sn_{13}$.

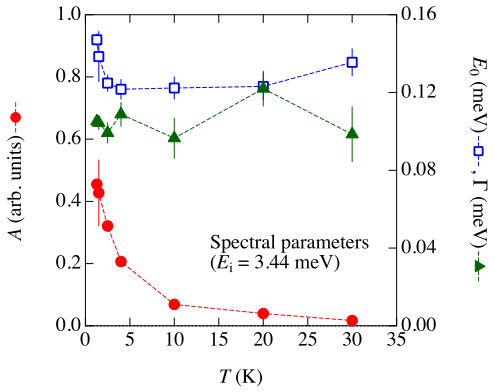

FIG. 8. Temperature dependencies of the fitting parameters for the $E_{\rm i} = 3.44$ meV data. Spectral magnitude A, excitation peak position E_0, and spectral width Γ.

C. Specific heat

The C_p/T data of $Ce_3Rh_4Sn_{13}$ shown in Fig. 6 exhibits a characteristic temperature dependence with the broad maximum at $T = \sqrt{0.8} = 0.89$ K. The peak temperature can be attributed to the spin dynamics energy of 0.1 meV deduced from the low-energy INS results as described above. It is attractive that the $C_p \propto T^3$ behavior appears below the peak temperature, which is not owing to the phonon excitation but the electronic origin because as discussed quantitatively later the phonon specific-heat contribution is only in the order of 10^{-3} of that shown in Fig. 6. We performed a least-squares fitting analysis based on $C_p = \gamma T + \beta' T^3$ to the data below

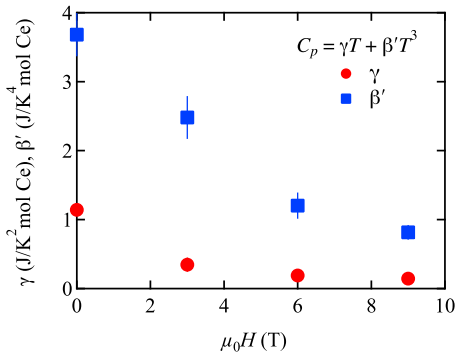

FIG. 9. Fitted parameters γ and β' for the electronic C_p/T shown in Fig. 6 as functions of the applied magnetic fields.

the maximum, the results of which are shown by solid lines in Fig. 6. The data below $T = \sqrt{0.5} = 0.7$ K are reproduced well by this formula, and the determined γ and β' against the applied magnetic fields are plotted in Fig. 9.

V. DISCUSSION

A. CEF schemes

The present INS data of $Ce_3Rh_4Sn_{13}$ show the multicomponent spectral shape, which is seen as asymmetric peak shape observed in the previous study [55], $Ce_3Co_4Sn_{13}$ [28], and $Ce_3Ir_4Sn_{13}$ [32]. The data accumulation with the three compounds verifies the two inequivalent level schemes in the chiral phase of $Ce_3T_4Sn_{13}$ (T = Co, Rh, and Ir). According to the present analysis of the CEF level schemes in $Ce_3Rh_4Sn_{13}$, the ground states are assigned to $\Gamma_6^{(2)}(\mp 0.7165|\pm 5/2\rangle \pm 0.6976|\mp 3/2\rangle)$ for scheme A and $\Gamma_6^{(2)}(\mp 0.7218|\pm 5/2\rangle \pm 0.6854|\mp 3/2\rangle)$ for scheme B. These two sites carry magnetic-moment eigenvalues (quantization axis component) of 0.474 and 0.532 μ_B/Ce, respectively. Previously published data of the field-dependent magnetization, $M(H)$, at 2 K shows a saturation behavior with applied magnetic fields, and reaches 0.73 μ_B/Ce at 5 T [66]. Based on the present CEF schemes A and B for $Ce_3Rh_4Sn_{13}$, the magnetization along the x and y axes are higher than that along the z axis. The three Ce1 and Ce2 linear rows are along the cubic principal fourfold rotation axes, and orthogonal in the crystal structure shown in Fig. 1. The quantization z axis corresponds to the row direction. Therefore, the measured magnetization is assumed to be the averaged magnitude under magnetic fields along these principal axes ([1 0 0], [0 1 0], or [0 0 1]), which becomes 0.755 μ_B/Ce. Because the value is close to the literature data, validity of the present CEF schemes is confirmed.

B. Low-energy spin excitation

As deduced in the previous sections, the magnetic excitation was observed in the low-energy region of $Ce_3Rh_4Sn_{13}$, which is associated with the Kramers doublet CEF ground state. This excitation is characterized by the inelastic peak at 0.1 meV and an extended spectrum up to 0.5 meV, which is not fully described by quasielastic scattering responses often observed for the conventional HF state. It is a key phenomenon that this excitation produces the broad peak of magnetic specific heat located at 0.8 K. Hence, the Ce-ion $4f$-electron state clearly contributes to the electronic specific heat that will be discussed later in terms of the Weyl fermions.

Adroja *et al.* also reported the low-energy spin dynamics for $Ce_3Rh_4Sn_{13}$ [55]. Their analysis reproduced the spectrum by a combination between the quasielastic peak with the 0.05 meV width and the inelastic peak at 0.18 meV with 0.11 meV width. Our analysis does not require the quasielastic component, but the inelastic part is consistent between the two studies. Adroja *et al.* mentioned that the short-range magnetic correlation lifts degeneracy of the CEF Kramers doublet ground state. However, no clear momentum dependence was observed in the present experiment at 1.3 K; thus, the intersite interaction cannot be deduced for $Ce_3Rh_4Sn_{13}$. Since the lowest measuring temperature corresponds to the characteristic excitation energy, a thermal fluctuation might give rise to a local dynamics. Another reason for the less Q-dependent spectrum is a very gradual dispersion relation that cannot be resolved by the present INS spectroscopy. In contrast, the dispersion relation of AFM spin dynamics in $Ce_3Co_4Sn_{13}$ extends to the excitation energy of 0.5 meV or larger at the Brillouin zone boundary with respect to the $I2_13$ structure in I′ phase. Furthermore, the AFM ordering of tiny magnetic-moment amplitude was found in $Ce_3Ir_4Sn_{13}$. The various spatial magnetic correlations may indicate that the $Ce_3T_4Sn_{13}$ compounds are in the vicinity of magnetic quantum criticality.

C. Weyl–Kondo semimetal in chiral phase

As written in the results part, we have claimed that C_p of $Ce_3Rh_4Sn_{13}$ is much larger than that of $La_3Rh_4Sn_{13}$, and the electronic specific heat dominates below 0.63 K. Hereafter we will discuss this point in detail. Specific-heat data of $La_3Rh_4Sn_{13}$ reported in the literature obeys $C_p/T = \gamma + \beta T^2$ with $\gamma = 13.5$ mJ mol^{-1} K^{-2} and $\beta = 7.5$ mJ mol^{-1} K^{-4} [20,21]. As described in the references, if we hypothesize $\beta = (12/5)Rn\pi^4\theta_D^{-3}$ for phonon contribution based on the Debye model, where n is the number of atoms in a formula unit and R is the gas constant, the Debye temperature θ_D was estimated to be 173 K.

To deduce the phonon energy of $Ce_3Rh_4Sn_{13}$, we measured a phonon spectrum of a polycrystalline sample of the same series compound $Ce_3Ru_4Sn_{13}$, as shown in the Supplemental Material [33,53]. The Ru-based compound does not show the structural phase transition, and no phonon anomaly appears in contrast to $Ce_3Rh_4Sn_{13}$. However, the phonon data of the Ru-based compound can be used to estimate the order of magnitude of θ_D that is expected to be determined by the low-energy boundary of optical modes. The local maximum of spectral weight seen at 5.4 meV is caused by phonon mode because the intensity becomes stronger at higher temperatures. This excitation corresponds to $\theta_D = 63$ K of phonon density-of-state (van Hove singularity) owing to the lowest-energy boundary of optical modes of $Ce_3Ru_4Sn_{13}$. Since the crystal structure of the 3–4–13 compounds is complicated, several van Hove singularities should appear above 5.4 meV. The whole contributions of phonon modes give an averaged value $\theta_D = 173$ K evaluated from the specific-heat data. The estimated θ_D values are much larger than that of the temperature

range of the T^3 behavior. Furthermore, if we suppose $\theta_D =$ 63 K corresponding to the observed lowest van Hove singularity energy of $Ce_3Ru_4Sn_{13}$ instead of $\theta_D = 173$ K giving $\beta = 7.5$ mJ mol^{-1} K^{-4} for $La_3Ru_4Sn_{13}$, β is estimated to be 0.155 J mol^{-1} K^{-4}. Because this value is considerably smaller than $\beta' = 3.68$ J mol^{-1} K^{-4} of $Ce_3Rh_4Sn_{13}$, contribution of the phonon excitation is ignorable in the low-temperature specific heat of $Ce_3Rh_4Sn_{13}$, and the T^3 behavior is attributed to the Weyl fermion state.

In the present INS measurements for $Ce_3Rh_4Sn_{13}$, we evidenced the emergence of the spin fluctuation with the characteristic energy of 0.1 meV which can be attributed to the $4f$ electron state. In particular, the electronic bands comprised of hybridization between $4f$ and conduction electrons (c-f hybridization), which is supported by the XPS results, is expected to play a critical role in the anomalously enhanced T^3 term in the specific heat at low temperatures, as shown in Fig. 6. According to the study on $Ce_3Bi_4Pd_3$, the Weyl–Kondo semimetal is concluded from the linear band structure $\epsilon_{\boldsymbol{k}} = \hbar v^* k$ ($\omega_{\boldsymbol{k}} = v^* k$), where v^* corresponds to a quasiparticle velocity, and a resultant specific heat per unit volume $C_p = \frac{7\pi^2}{30} k_B (\frac{k_B T}{\hbar v^*})^3$, where $v^* = 885$ m/s [8–11]. Considering the Kondo-effect behavior in $Ce_3Bi_4Pd_3$ and $Ce_3Rh_4Sn_{13}$, the T^3 behavior of C_p is explained by the topologically protected linear electronic band associated with the c-f hybridization. The determined coefficient β' value for the T^3 term of C_p at zero magnetic field for $Ce_3Rh_4Sn_{13}$ gives $v^* = 104.5$ m/s. This quasiparticle velocity and the linear band structure give an excitation energy approximately equal to $\hbar v^* 2\pi/a' =$ 0.2 meV at the Brillouin zone boundary ($k = 2\pi/a'$) of the $I2_13$ structure in I′ phase. This magnitude is comparable to the characteristic parameters E_0 and Γ of the low-energy magnetic excitation (Fig. 8). Although such a small excitation energy variation in the momentum space is too difficult to be resolved by the present spectroscopic resolution, the present experimental facts support the Weyl–Kondo semimetal behavior in $Ce_3Rh_4Sn_{13}$.

The velocity v^* of $Ce_3Rh_4Sn_{13}$ is lower than that of $Ce_3Bi_4Pd_3$, and the more flat linear band structure is expected to arise in $Ce_3Rh_4Sn_{13}$. The flat band means that the slight change in the Fermi level (the conduction electron density, for example) gives rise to the drastic change in the Fermi surface area or the conductivity. Therefore, the different electrical resistivity between $Ce_3Rh_4Sn_{13}$ and $La_3Rh_4Sn_{13}$ is caused in part by such a sensitive carrier state on the flat topological linear band, although the c-f hybridization also contributes to the electronic band property in the Ce-based compound. The deviation in C_p from the T^3 behavior above $\sqrt{0.4} = 0.63$ K is explained by a shift of electrons from the topological linear band caused by thermal excitation accompanied with suppression of the spin dynamics.

Applying magnetic fields diminishes β' and increases v^*, as shown in Fig. 6. Magnetic fields lift the Kramers doublet degeneracy and the characteristic spin dynamics, and its contribution to specific heat should be suppressed; thus, β' is diminished. Actually, as demonstrated in a previous study, the specific heat peak temperature above 3 T is proportional to applied magnetic field magnitude, which can be explained by the Zeeman split of the CEF doublet [20]. This phenomenon indicates that the spin dynamics appearing in the Weyl–Kondo state crosses over to the CEF splitting characterized by a localized $4f$ behavior under applied magnetic fields. Such a crossover of the $4f$ state also accompanies modification of the conduction electron state, and the Fermi level may move to a steeper dispersion point; then, v^* increases. In contrast, the magnetic-field dependence of v^* of $Ce_3Bi_4Pd_3$ is opposite to $Ce_3Rh_4Sn_{13}$ [10]. The variation of v^* with respect to magnetic fields depends on materials, and should be determined by the band structure and the carrier character.

VI. CONCLUSION

The Ce $4f$ electronic state in the chiral-lattice phase of $Ce_3Rh_4Sn_{13}$ has been revealed via INS, specific-heat, and XPS measurements. The entire INS spectrum is reproduced by the two CEF level schemes, which are attributed to the inequivalent Wyckoff sites in the chiral structure [30]. The spin dynamics evolves in the low-energy Kramers doublets, which causes the specific heat obeying $\gamma T + \beta' T^3$. The XPS data support that the Ce $4f$ electrons are hybridized with the conduction electrons, which contribute to the aforementioned spin fluctuations and specific heat. The results give an evidence of the Weyl–Kondo semimetal state in this compound, as was proposed for $Ce_3Bi_4Pd_3$ [8–11]. Further studies are necessary to resolve the detailed electronic band structure and transport property. $Ce_3T_4Sn_{13}$ (T = Co, Rh, and Ir) undergo the chiral $I2_13$ structural phase transition, which can be suppressed by atomic substitution [53]. Hence, it is a further issue to approach a quantum critical point owing to the chiral symmetry fluctuation, at which unconventional electronic phenomena are expected to be induced by the low-lying Weyl fermions beyond the well-known non-Fermi-liquid behaviors and spin-liquid states.

ACKNOWLEDGMENTS

We thank Y. Otomo, K. Tomiyasu, and M. Onodera at Tohoku University for their collaborations for the sample synthesis and neutron scattering experiments. T. Kikuchi and Y. Inamura at J-PARC Center are acknowledged for their assistance in the analysis of AMATERAS data. S. Nakazato, D. Hashimoto, M. Shiozawa, Rahmanto, and K. Suzuki at Ibaraki University are acknowledged for their assistance in the XAS and XPS experiments. D. T. Adroja and K. Kaneko are acknowledged for fruitful discussions of the studies on the 3–4–13 series compounds. This study was supported in part by the Japan Society for the Promotion of Science, KAKENHI Grants No. JP21224008 [Scientific Research (S)], No. JP23244068 [Scientific Research (A)], No. JP24654080 [Exploratory Research], No. JP15H03692 [Scientific Research (B)], No. JP17H05209 [Scientific Research on Innovative Areas "3D Active-Site Science"], No. JP18H01182 [Scientific Research (B)], No. JP20H01848 [Scientific Research (B)], and the Yamada Science Foundation. The experiment at AMATERAS (BL14) of J-PARC MLF was conducted under approved proposals No. 2016A0063 and No. 2019B0080, and that at ThALES of ILL No. 4-05-623. The XAS and XPS experiments at BL23SU of SPring-8 were conducted under a collaboration contract between Ibaraki University and JAEA.

[1] T. Kasuya and T. Saso (eds.), *Theory of Heavy Fermions and Valence Fluctuations* (Springer, Heidelberg, 1985).

[2] N. Grewe and F. Steglich, *Handbook on the Physics and Chemistry of Rare Earths* (Elsevier, New York, 1991), Vol. 14, Chap. 97, pp. 343–474.

[3] T. Takimoto, J. Phys. Soc. Jpn. **80**, 123710 (2011).

[4] H. Weng, J. Zhao, Z. Wang, Z. Fang, and X. Dai, Phys. Rev. Lett. **112**, 016403 (2014).

[5] Y. Sato, Z. Xiang, Y. Kasahara, T. Taniguchi, S. Kasahara, L. Chen, T. Asaba, C. Tinsman, H. Murayama, O. Tanaka, Y. Mizukami, T. Shibauchi, F. Iga, J. Singleton, Lu Li, and Y. Matsuda, Nat. Phys. **15**, 954 (2019).

[6] J. L. Mañes, Phys. Rev. B **85**, 155118 (2012).

[7] H. Weng, C. Fang, Z. Fang, B. A. Bernevig, and X. Dai, Phys. Rev. X **5**, 011029 (2015).

[8] H.-H. Lai, S. E. Grefe, S. Paschen, and Q. Si, Proc. Natl. Acad. Sci. USA **115**, 93 (2018).

[9] S. E. Grefe, H.-H. Lai, S. Paschen, and Q. Si, Phys. Rev. B **101**, 075138 (2020).

[10] S. Dzsaber, L. Prochaska, A. Sidorenko, G. Eguchi, R. Svagera, M. Waas, A. Prokofiev, Q. Si, and S. Paschen, Phys. Rev. Lett. **118**, 246601 (2017).

[11] S. Dzsaber, X. Yan, M. Taupin, G. Eguchi, A. Prokofiev, T. Shiroka, P. Blaha, O. Rubel, S. E. Grefe, H.-H. Lai, Q. Si, and S. Paschen, Proc. Natl. Acad. Sci. USA **118**, e2013386118 (2021).

[12] A. K. Mitchell and L. Fritz, Phys. Rev. B **92**, 121109(R) (2015).

[13] H.-R. Chang, J. Zhou, S.-X. Wang, W.-Y. Shan, and D. Xiao, Phys. Rev. B **92**, 241103(R) (2015).

[14] A. L. Cornelius, A. D. Christianson, J. L. Lawrence, V. Fritsch, E. D. Bauer, J. L. Sarrao, J. D. Thompson, and P. G. Pagliuso, Phys. B: Condens. Matter **378-380**, 113 (2006).

[15] E. L. Thomas, H.-O. Lee, A. N. Bankston, S. MaQuilon, P. Klavins, M. Moldovan, D. P. Young, Z. Fisk, and J. Y. Chan, J. Solid State Chem. **179**, 1642 (2006).

[16] J. R. Collave, H. A. Borges, S. M. Ramos, E. N. Hering, M. B. Fontes, E. Baggio-Saitovitch, L. Mendonça-Ferreira, E. M. Bittar, and P. G. Pagliuso, J. Appl. Phys. **117**, 17E307 (2015).

[17] A. Ślebarski, B. D. White, M. Fijałkowski, J. Goraus, J. J. Hamlin, and M. B. Maple, Phys. Rev. B **86**, 205113 (2012).

[18] A. Ślebarski and J. Goraus, Phys. Rev. B **88**, 155122 (2013).

[19] Y. Ōduchi, C. Tonohiro, A. Thamizhavel, H. Nakashima, S. Morimoto, T. D. Matsuda, Y. Haga, K. Sugiyama, T. Takeuchi, R. Settai, M. Hagiwara, and Y. Ōnuki, J. Magn. Magn. Mater. **310**, 249 (2007).

[20] U. Köhler, A. P. Pikul, N. Oeschler, T. Westerkamp, A. M. Strydom, and F. Steglich, J. Phys.: Condens. Matter **19**, 386207 (2007).

[21] M. Gamża, W. Schnelle, A. Ślebarski, U. Burkhardt, R. Gumeniuk, and H. Rosner, J. Phys.: Condens. Matter **20**, 395208 (2008).

[22] H. Sato, T. Fukuhara, S. Iwakawa, Y. Aoki, I. Sakamoto, S. Takayanagi, and N. Wada, Phys. B: Condens. Matter **186-188**, 630 (1993).

[23] S. Takayanagi, H. Sato, T. Fukuhara, and N. Wada, Phys. B: Condens. Matter **199-200**, 49 (1994).

[24] J. R. Collave, H. A. Borges, S. M. Ramos, E. N. Hering, M. B. Fontes, E. Baggio-Saitovitch, A. Eichler, E. M. Bittar, and P. G. Pagliuso, Solid State Commun. **177**, 132 (2014).

[25] N. Kase, H. Hayamizu, and J. Akimitsu, Phys. Rev. B **83**, 184509 (2011).

[26] H. Hayamizu, N. Kase, and J. Akimitsu, Phys. C: Supercond. Appl. **470**, S541 (2010).

[27] N. Kase, H. Hayamizu, K. Inoue, and J. Akimitsu, Phys. C: Supercond. Appl. **471**, 711 (2011).

[28] K. Iwasa, Y. Otomo, K. Suyama, K. Tomiyasu, S. Ohira-Kawamura, K. Nakajima, and J.-M. Mignot, Phys. Rev. B **95**, 195156 (2017).

[29] A. D. Christianson, J. S. Gardner, H. J. Kang, J.-H. Chung, S. Bobev, J. L. Sarrao, and J. M. Lawrence, J. Magn. Magn. Mater. **310**, 266 (2007).

[30] K. Suyama, K. Iwasa, Y. Otomo, K. Tomiyasu, H. Sagayama, R. Sagayama, H. Nakao, R. Kumai, Y. Kitajima, F. Damay, J.-M. Mignot, A. Yamada, T. D. Matsuda, and Y. Aoki, Phys. Rev. B **97**, 235138 (2018).

[31] S. Nakazato, K. Iwasa, D. Hashimoto, M. Shiozawa, K. Kuwahara, H. Nakao, H. Sagayama, M. Ishikado, T. Ohhara, A. Nakao, K. Munakata, Koji, and R. Kiyanagi, JPS Conf. Proc. **30**, 011128 (2020).

[32] K. Iwasa, S. Nakazato, D. Hashimoto, M. Shiozawa, K. Kuwahara, H. Sagayama, S. Ohira-Kawamura, N. Murai, D. T. Adroja, and A. M. Strydom, J. Phys. Soc. Jpn. **90**, 124701 (2021).

[33] See Supplemental Material at http://link.aps.org/supplemental/10.1103/PhysRevMaterials.7.014201 for the summary of crystal structure investigations of the $Ln_3T_4Sn_{13}$ series compounds and for the details of INS data obtained at AMATERAS (BL14) of MLF, J-PARC.

[34] G. P. Espinosa, Mater. Res. Bull. **15**, 791 (1980).

[35] J. L. Hodeau, M. Marezio, J. P. Remeika, and C. H. Chen, Solid State Commun. **42**, 97 (1982).

[36] S. Miraglia, J. L. Hodeau, M. Marezio, C. Laviron, M. Ghedira, and G. P. Espinosa, J. Solid State Chem. **63**, 358 (1986).

[37] L. E. Klintberg, S. K. Goh, P. L. Alireza, P. J. Saines, D. A. Tompsett, P. W. Logg, J. Yang, B. Chen, K. Yoshimura, and F. M. Grosche, Phys. Rev. Lett. **109**, 237008 (2012).

[38] S. K. Goh, D. A. Tompsett, P. J. Saines, H. C. Chang, T. Matsumoto, M. Imai, K. Yoshimura, and F. M. Grosche, Phys. Rev. Lett. **114**, 097002 (2015).

[39] W. C. Yu, Y. W. Cheung, P. J. Saines, M. Imai, T. Matsumoto, C. Michioka, K. Yoshimura, and S. K. Goh, Phys. Rev. Lett. **115**, 207003 (2015).

[40] D. A. Tompsett, Phys. Rev. B. **89**, 075117 (2014).

[41] D. G. Mazzone, S. Gerber, J. L. Gavilano, R. Sibille, M. Medarde, B. Delley, M. Ramakrishnan, M. Neugebauer, L. P. Regnault, D. Chernyshov, A. Piovano, T. M. Fernández-Díaz, L. Keller, A. Cervellino, E. Pomjakushina, K. Conder, and M. Kenzelmann, Phys. Rev. B **92**, 024101 (2015).

[42] I. W. H. Oswald, B. K. Rai, G. T. McCandless, E. Morosan, and J. Y. Chan, Cryst. Eng. Commun. **19**, 3381 (2017).

[43] J. Welsch, S. Ramakrishnan, C. Eisele, N. van Well, A. Schönleber, S. van Smaalen, S. Matteppanavar, A. Thamizhavel, M. Tolkiehn, C. Paulmann, and S. Ramakrishnan, Phys. Rev. Mater. **3**, 125003 (2019).

[44] P. Bordet, D. E. Cox, G. P. Espinosa, J. L. Hodeau, and M. Marezio, Solid State Commun. **78**, 359 (1991).

[45] C. N. Kuo, W. T. Chen, C. W. Tseng, C. J. Hsu, R. Y. Huang, F. C. Chou, Y. K. Kuo, and C. S. Lue, Phys. Rev. B **97**, 094101 (2018).

[46] Y. Otomo, K. Iwasa, K. Suyama, K. Tomiyasu, H. Sagayama, R. Sagayama, H. Nakao, R. Kumai, and Y. Murakami, Phys. Rev. B **94**, 075109 (2016).
[47] K. Momma and F. Izumi, J. Appl. Crystallogr. **41**, 653 (2008).
[48] J. P. Remeika, G. P. Espinosa, A. S. Cooper, H. Barz, J. M. Rowell, D. B. McWhan, J. M. Vandenberg, D. E. Moncton, Z. Fisk, L. D. Woolf, H. C. Hamaker, M. B. Maple, G. Shirane, and W. Thomlinson, Solid State Commun. **34**, 923 (1980).
[49] G. P. Espinosa, A. S. Cooper, and H. Barz, Mater. Res. Bull. **17**, 963 (1982).
[50] K. Nakajima, S. Ohira-Kawamura, T. Kikuchi, M. Nakamura, R. Kajimoto, Y. Inamura, N. Takahashi, K. Aizawa, K. Suzuya, K. Shibata, T. Nakatani, K. Soyama, R. Maruyama, H. Tanaka, W. Kambara, T. Iwahashi, Y. Itoh, T. Osakabe, S. Wakimoto, K. Kakurai *et al.*, J. Phys. Soc. Jpn. **80**, SB028 (2011).
[51] Y. Inamura, T. Nakatani, J. Suzuki, and T. Otomo, J. Phys. Soc. Jpn. **82**, SA031 (2013).
[52] E. J. Lisher and J. B. Forsyth, Acta. Crystallogr. Sect. A **27**, 545 (1971).
[53] D. Hashimoto, K. Iwasa, M. Shiozawa, K. Kuwahara, S. Ohira-Kawamura, N. Murai, and K. Nakajima (unpublished).
[54] K. Iwasa, K. Kuwahara, H. Sagayama, S. Ohira-Kawamura, T. Kikuchi, K. Nakajima, and M. Ishikado (unpublished).
[55] D. T. Adroja, A. M. Strydom, A. P. Murani, W. A. Kockelmann, and A. Fraile, Phys. B: Condens. Matter **403**, 898 (2008).
[56] K. Iwasa, L. Hao, K. Kuwahara, M. Kohgi, S. R. Saha, H. Sugawara, Y. Aoki, H. Sato, T. Tayama, and T. Sakakibara, Phys. Rev. B **72**, 024414 (2005).
[57] J. Otsuki, H. Kusunose, and Y. Kuramoto, J. Phys. Soc. Jpn. **74**, 200 (2005).
[58] K. Iwasa, L. Hao, T. Hasegawa, T. Takagi, K. Horiuchi, Y. Mori, Y. Murakami, K. Kuwahara, M. Kohgi, H. Sugawara, S. R. Saha, Y. Aoki, and H. Sato, J. Phys. Soc. Jpn. **74**, 1930 (2005).
[59] K. Iwasa, J.-M. Mignot, S. Raymond, P. Steffens, and K. Suyama, Magnetic excitations in electron-mass-enhanced semiconductors $Ce_3Co_4Sn_{13}$ and $Ce_3Rh_4Sn_{13}$ (Institut Laue–Langevin (ILL), 2015), https://doi.ill.fr/10.5291/ILL-DATA.4-05-623.
[60] O. Gunnarsson and K. Schönhammer, Phys. Rev. B **28**, 4315 (1983).
[61] U. Walter, J. Phys. Chem. Solids **45**, 401 (1984).
[62] W. Marshall and R. D. Lowde, Rep. Prog. Phys. **31**, 705 (1968).
[63] M. Arai, A. D. Taylor, S. M. Bennington, Z. A. Bowden, R. Osborn, M. Kohgi, K. Ohoyama, and T. Nakane, Proc. ICANS-XI, 644 (1990).
[64] R. Kajimoto, K. Sato, Y. Inamura, and M. Fujita, AIP Conf. Proc. **1969**, 050004 (2018).
[65] G. Aeppli and C. Broholm, in *Handbook on the Physics and Chemistry of Rare Earths*, edited by K. A. Gschneidner, Jr., L. Eyring, G. H. Lander, and G. R. Choppin (Elsevier Science B. V., North-Holland, 1994), Vol. 19, pp. 123–175.
[66] D. Niepmann, R. Pöttgen, K. M. Poduska, F. J. DiSalvo, H. Trill, and B. D. Mosel, Z. Naturforsch. Teil B **56**, 1 (2001).